Structural and molecular basis of cross-seeding barriers in amyloids

Asen Daskalov, Denis Martinez, Virginie Coustou, Nadia El Mammeri, Mélanie Berbon, Loren B. Andreas, Benjamin Bardiaux, Jan Stanek, Abdelmajid Noubhani, Brice Kauffmann, et al.

Structural and molecular basis of cross-seeding barriers in amyloids

Asen Daskalov[a,b,1], Denis Martinez [a,1], Virginie Coustou[b], Nadia El Mammeri[a], Mélanie Berbon[a], Loren B. Andreas[d,2], Benjamin Bardiaux[c], Jan Stanek[d], Abdelmajid Noubhani[a], Brice Kauffmann[e], Joseph S. Wall[f], Guido Pintacuda[d], Sven J. Saupe[b*], Birgit Habenstein[a*], Antoine Loquet[a*]

a Univ. Bordeaux, CNRS, CBMN UMR 5348, IECB, F-33600 Pessac, France
b Univ. Bordeaux, CNRS, IBGC UMR 5095, F-33077 Bordeaux, France
c Structural Bioinformatics Unit, CNRS UMR 3528, Institut Pasteur, F-75015 Paris, France
d Centre de RMN à Très Hauts Champs, Université de Lyon (CNRS/ENS de Lyon/UCB-Lyon 1), F-69100 Villeurbanne, France
e Univ. Bordeaux, CNRS, INSERM, IECB, UMS 3033, F-33600 Pessac, France
f Brookhaven National Laboratory, Upton, NY 11973-5000

[1] contributed equally to this work

[2] present address: Max Planck Institute for Biophysical Chemistry, Am Fassberg 11, D-37077 Göttingen, Germany.

Corresponding authors

Antoine Loquet
Institute of Chemistry and Biology of Membranes and Nanoobjects, Institut Européen de Chimie et Biologie (CNRS UMR 5248, Université de Bordeaux), 33600 Pessac, France
a.loquet@iecb.u-bordeaux.fr

Birgit Habenstein
Institute of Chemistry and Biology of Membranes and Nanoobjects, Institut Européen de Chimie et Biologie (CNRS UMR 5248, Université de Bordeaux), 33600 Pessac, France
b.habenstein@iecb.u-bordeaux.fr

Sven J. Saupe

Non-Self Recognition in Fungi, Institut de Biochimie et de Génétique Cellulaire (CNRS UMR 5095, Université de Bordeaux), 33077 Bordeaux, France

sven.saupe@ibgc.cnrs.fr

Classification

Major Category: Biological Sciences

Minor Category: Microbiology

Abstract

Neurodegenerative disorders are frequently associated with β-sheet-rich amyloid deposits. Amyloid-forming proteins can aggregate under different structural conformations known as strains, which can exhibit a prion-like behaviour and distinct patho-phenotypes. Precise molecular determinants defining strain specificity and cross-strain interactions (cross-seeding) are currently unknown. The HET-s prion protein from the fungus *Podospora anserina* represents a model system to study the fundamental properties of prion amyloids. Here, we report the amyloid prion structure of HELLF, a distant homolog of the model prion HET-s. We find that these two amyloids, sharing only 17% sequence identity, have nearly identical β-solenoid folds but lack cross-seeding ability *in vivo*, indicating that prion specificity can differ in extremely similar amyloid folds. We engineer the HELLF sequence to explore the limits of the sequence-to-fold conservation and to pinpoint determinants of cross-seeding and prion specificity. We find that amyloid fold conservation occurs even at an exceedingly low level of identity to HET-s (5%). Next, we derive a HELLF-based sequence, termed HEC, able to breach the cross-seeding barrier *in vivo* between HELLF and HET-s, unveiling determinants controlling cross-seeding at residue level. These findings show that virtually identical amyloid backbone structures might not be sufficient for cross-seeding and that critical side-chain positions could determine the seeding specificity of an amyloid fold. Our work redefines the conceptual boundaries of prion strain and sheds light on key molecular features concerning an important class of pathogenic agents.

Keywords: Amyloid; prion; sequence-to-fold; cross-seeding; nuclear magnetic resonance

Significance

Amyloid folds, while performing functional roles in most domains of life, remain a key factor in the emergence and development of multiple neurodegenerative disorders in humans. The significance of our study is twofold: first, by structurally characterizing highly divergent natural prion amyloids, we uncovered that functional amyloids can evolve in a regime of fold conservation, withstanding extreme sequence diversification. Second, we found that virtually identical amyloid backbone structures might not be sufficient for cross-seeding and that key side-chain positions could determine the seeding specificity of an amyloid fold. This work thus sheds light on the fundamental properties of a major category of pathogenic agents.

Introduction

Amyloid-forming proteins undergo a phase transition to form insoluble, polymeric assemblies, which can self-propagate *in vivo* as prions (1–3). Amyloid aggregates associated with neurodegenerative diseases (i.e. Alzheimer's, Parkinson's etc.) have a prion-like behaviour (4, 5) and can propagate under different structural conformations also known as prion 'strains' (conformational variants of identical protein sequence), which may be associated with distinct phenotypes of the pathology (6–9). The cross-talk between an infectious amyloid conformation (prion strain) and a naive homologous or heterologous amyloidogenic sequence, referred to as 'cross-seeding' (10, 11), is a critical event in prion biology, representing the key aspect of infectivity. Amyloid cross-seeding could play a role in the aetiology (12) and pathogenesis of various proteinopathies (13, 14). However, our understanding of the precise molecular and structural determinants allowing or limiting cross-seeding remains poor.

The fungal HET-s protein constitutes a highly favourable system to study the fundamental properties of prion amyloids, as a high-resolution structure of the propagative prion state is available (15, 16). The prion-forming domain (PFD) of HET-s contains two 21 amino acid pseudo-repeats (R1 and R2), which are alternately stacked, each repeat forming four β-strands, adopting a left-handed β-solenoid fold (15, 16). Noteworthy, several reports have stressed structural similarities between the HET-s amyloid fold and pathological amyloids formed by the human prion protein PrP (17) and tau (18).

Despite the structural similarities with some pathological amyloids, HET-s represents a functional amyloid, which is integral to an immunity-related signal transduction pathway in fungi (19). The β-solenoid fold ensures signal transduction from an activated NOD-like receptor (NLR) to a downstream execution protein (HET-S, a pore-forming variant of the HET-s prion protein). The fold represents a cell death trigger and functions on the basis of the prion principle (19, 20). The structural templating of the HET-S PFD into the amyloid fold triggers the cytotoxicity of the α-helical HeLo domain, which induces cell death targeting the plasma membrane (21–23). Signal-transducing amyloids are widespread in fungi (24) and at least five

subfamilies of HET-s-related amyloid motifs (HRAMs) have been identified (25). The HRAMs exhibit the two pseudo-repeats organization of HET-s and a specific pattern of hydrophobic and polar amino acids, while each subfamily is being defined by the conservation of a set of HRAM-specific residues (25). It has been speculated that the HRAMs may share a common β-solenoid fold and that natural diversification is driven to preserve specificity of the signalling pathways (between NLRs and cognate effectors) by limiting amyloid cross-seeding between distinct HRAMs (19, 25). Here, we use the HRAMs as an experimental framework to investigate 1) the sequence-to-fold relation in prion amyloids and 2) the molecular determinants defining prion specificity, which allow or prevent cross-seeding.

Results

Molecular characterization of HELLF

We chose to work with a newly identified HELLF protein, encoded in the genome of *Podospora anserina* (*SI Appendix*, Fig. S1), the natural host of the [Het-s] prion. HELLF consists of an N-terminal HELL (HeLo-like) domain and a putative C-terminal PFD. The HELLF PFD carries strongly divergent HRAM pseudo-repeats (R1 and R2) showing only 17% of sequence identity with the PFD repeats of HET-S/s (Fig. 1A; *SI Appendix,* Fig. S1). HELLF pseudo-repeats belong to the HRAM5 family (Fig. 1B). Strains expressing HELLF(209-277) showed phenotypic bistability exhibiting either a [Φ*] phenotype, where the protein remains soluble or a [Φ] phenotype with formation of dot-like aggregates (Fig. 1C; *SI Appendix*, Fig. S1). The [Φ] strains triggered cell death upon anastomosis (cellular fusion) with strains expressing full-length HELLF, while [Φ*] strains formed viable heterokaryons (Fig. 1D). During the cell death reaction, as described for HET-S (22), HELLF relocates to the cell membrane (*SI Appendix*, Fig. S1). The [Φ*] strains (aggregates-free) switched spontaneously (~24 hours) to [Φ] strains (with aggregates), which in turn could be cured (or reversed) back to [Φ*] state through a sexual cross (*SI Appendix*, Table S1, Table S2). These results establish HELLF as a distant HET-S homolog and demonstrate that the HRAM5 pseudo-repeats bearing PFD of HELLF behaves as a prion in *P. anserina*.

Solid-state NMR (ssNMR) structure of HELLF prion domain

We engaged in the structural characterization of HELLF(209-277). The protein self-assembled into unbranched fibrils *in vitro* (Fig. 1E), exhibiting a typical cross-β signature by X-ray diffraction (*SI Appendix*, Fig. S2). We took advantage of recent developments for fast magic-angle spinning (MAS) NMR probes (26–28) to establish, and implement for the first time on a fibril sample, a three-dimensional (3D) structure determination approach, based entirely on ^{1}H-^{1}H proximities. The approach, reminiscent of nuclear Overhauser effect (nOe)-based solution NMR methods to solve soluble globular protein structures, allows a tremendous gain in sensitivity and enables the use of simplified labelling schemes and minimal sample quantities.

Approximately 300μg of fully protonated HELLF(209-277) were packed into a 0.7 mm ssNMR rotor (Fig. 2A). Ultra-fast MAS performed at rates of ~110 kHz allowed the acquisition of high-resolution ^{1}H-detected multidimensional spectra even in fully protonated samples (Fig. 2B; *SI Appendix*, Fig. S3) with ^{1}H line widths of ~150-200Hz enabling assignment of backbone and side-chain protons (29). A unique set of resonances revealed the presence of a single conformational polymorph in the fibrillar assembly, and conformation-dependent chemical shifts (30) revealed a β-rich rigid core extending from residue Q221 to S272, including 8 β-strands (Fig. S4). A flexible linker segment (G240-D247), comprising a β-breaker GxxxPG motif, subdivides the rigid core in 2 regions with 4 β-strands each (Fig. S4). We employed a combination of 3D H(H)CH and H(H)NH experiments (27) on a fully protonated, uniformly ^{13}C,^{15}N-labeled sample to derive 178 internuclear ^{1}H-^{1}H distances (Fig. 2C). 3D amyloid architectures render the distinction between intra- and intermolecular contacts in ssNMR experiments difficult and usually require complex labelling schemes (16, 31). We designed a new and simple labelling strategy based on an equimolar mixture of fully protonated proteins at natural abundance, randomly co-aggregated with deuterated, extensively amide-reprotonated and uniformly ^{15}N-labeled proteins (scheme denoted as (1/1) [(U-^{1}H,^{14}N)/(U-^{1}H^{N},^{2}H,^{15}N)]) (Fig. 2E). Using this scheme, we observed 33 intermolecular ^{1}H-^{1}H inter-strand aliphatic to amide distances relying on a single 3D H(H)NH spectrum (Fig. 2D) with an asymmetric polarization

transfer (Fig. 2F). We identified 211 distance restraints in total, of which 176 are long-range restraints (|i-j| > 4) (Fig. 2G) to derive a 3D structure of the HELLF fibrillar assembly at atomic resolution with 20-conformer bundle r.m.s.d of 0.73Å for backbone atoms and 1.18Å for heavy atoms (Fig. 3; *SI Appendix*, Table S3). Our 3D structure determination approach based on ^{1}H-^{1}H proximities compares favourably to benchmark studies of the HET-s prion domain amyloid structure by ssNMR (16); we detected approximately 4.5 structurally meaningful restraints per residue in the rigid amyloid core, a number approaching those used in high-resolution structure determination protocols in solution NMR.

HELLF and HET-s prions share an identical backbone β-solenoid core

The HELLF fibrillar architecture shows a β-solenoid fold, made by the intermolecular packing of HELLF monomers along the fibril axis (Fig. 3). The intramolecular HELLF fold is composed of 8 β-strand structural elements separated by a short unstructured region (Gly240-Asp247) (Fig. 3). Intramolecular ssNMR restraints reveal a regular and rigid core, constituted by alternate stacking of R1 (R1β_1 to R1β_4) and R2 (R2β_1 to R2β_4) pseudo-repeat regions (Fig. 4B, Fig. 3). Each pseudo-repeat adopts a triangular shape, stabilized by hydrophobic side-chains interlaced (*SI Appendix*, S5A) inside the amyloid core and protected from the solvent. Water molecules are excluded from the amyloid core (*SI Appendix*, S5B-C). Several β-breaker glycine residues allow for bending two consecutive β-arcs into the triangular arrangement of the amyloid core (Fig. 4B). R1 and R2 repeats are stacked through a hydrogen bond-rich pairing between β-sheets (R1β_i with R2β_i, T255/S232 and T228/S259). To corroborate the HELLF intramolecular R1/R2 stacking, we performed scanning transmission electron microscopy (STEM) mass-per-length (MPL) measurements and determined a MPL of 0.99±0.10 kDa/Å corresponding to 1.1±0.1 molecules per 0.94 nm (*SI Appendix*, Fig. S6). Considering a β-strand repetition of 0.47 nm in the cross-β architecture as measured by X-ray diffraction (*SI Appendix*, Fig. S2), it leads to a fibril layer (i.e. per 0.47 nm) composed of half of a HELLF molecule, in agreement with the fold determined by ssNMR (Fig. 2G, Fig. 3). The inter-subunit packing consists of parallel, pseudo in-register stacking and the overall intermolecular arrangement is consistent with cross-β stacked

219 solenoid architecture. In spite of the low sequence identity between HET-s and HELLF PFDs,
220 both prion domains adopt virtually identical backbone conformations (Fig. 4, A and C).
221 We took advantage of the high-resolution structures of HELLF and HET-s to perform molecular
222 modelling on the remaining HRAM families identified in fungal genomes (Fig. 4E). We found
223 that the observed sequence diversity in the HRAM superfamily is indeed compatible with a
224 unique structural solution underlying this amyloid fold (Fig. 4E). The findings underscore the
225 importance of the previously identified pattern of hydrophobic and polar amino acids as a
226 minimal requirement to adopt the HET-s-like β-solenoid fold (25).
227 In addition, we designed a protein sequence termed HED (HET-s distant) carrying two identical
228 repeats that share less than 5% identity with HET-s (one residue out of 21) (*SI Appendix*; Fig.
229 S7A, Table S5). HED was able to form a prion *in vivo* (*SI Appendix*, Fig. S7B-E). In vitro, HED
230 adopts a HET-s-like β-solenoid structure as seen by SSNMR (*SI Appendix*, Fig. S7F-G), implying a
231 β-solenoid fold conservation in spite of the extremely low sequence identity (5%) and a very
232 low sequence similarity (19%) to HET-s.
233 **HELLF and HET-s carry distinct prion specificities *in vivo***
234 Considering the structural similarity between HELLF and HET-s prion folds (Fig. 4A) and that
235 these proteins occur in the same species, we analysed the cross-seeding of [Φ] and [Het-s] prion
236 states *in vivo* (*SI Appendix*, Table S2). We found that [Φ] strains do not convert non-prion [Het-
237 s*] strains to the [Het-s] prion state nor do [Het-s] strains induce [Φ] prion formation (*SI*
238 *Appendix*, Table S2). HELLF PFD fibrils show no [Het-s] infectivity and HET-s PFD fibrils show
239 no [Φ] infectivity in transfection assays (*SI Appendix*, Table S4). HELLF and HET-s PFDs form
240 independent aggregates *in vivo* indicating that the two prions do not co-aggregate (Fig. 4D; *SI*
241 *Appendix*, Fig. S8). Strains co-expressing HELLF and HET-s can display four alternate epigenetic
242 states ([Het-s*] [Φ*], [Het-s] [Φ] but also [Het-s*] [Φ] and [Het-s] [Φ*]) confirming that [Het-s]
243 and [Φ] are independent prions (*SI Appendix*, Fig. S8, Table S2). Since the backbone structures
244 in the amyloid fold of HET-s and HELLF PFDs are nearly identical (Fig. 4A), it appears that

strong structural similarity and interactions of the cross-β backbones are insufficient for amyloid templating and/or co-aggregation.

At the level of side-chain packing, HELLF has more hydrophilic (Q^{221}, Q^{236}, Q^{248} and Q^{263}) side-chains pointing inside the amyloid core compared to HET-s (N^{226} and N^{262}). A striking difference is observed at the end of the 3rd β-strand, composed of $Q^{240}L$ (R1) and $L^{276}I$ (R2) in HET-s and $M^{235}Q$ (R1) and $F^{262}Q$ (R2) in HELLF. Therefore, the lack of cross-seeding between HET-s and HELLF could result from unfavourable hydrophobic-hydrophilic packing between solvent exposed HET-s Q^{240} and HELLF F^{262} as well as HET-s L^{241} and HELLF Q^{263}.

HRAM-specific residues control cross-seeding between HELLF and HET-s

The results suggested that side-chain residues, decorating the amyloid backbone, could play a key role in defining prion specificity and cross-seeding. Thus, we decided to test whether by varying HRAM-specific residues between HET-s and HELLF PFDs, the cross-seeding barrier between the two prions could be breached. We replaced five residues on each of the two 21 amino acids HRAM5 pseudo-repeats of HELLF with residues from the corresponding positions found in the HRAM1 pseudo-repeats of HET-s. The engineered sequence was termed HEC (HET-s closer). We targeted for replacement residues that are highly conserved inside each HRAM (Fig. 1.B) and essential for distinguishing HRAM5 (HELLF) from HRAM1 (HET-s) (25) (Fig. 5A). The five amino acid substitutions for each pseudo-repeat of HELLF were introduced in two strongly conserved HRAM5-specific sub-motifs of the protein – the QxFG (position 1-4, where x is any possible amino acid residue) and QG(Q/I) (position 16-18) sub-motifs (Fig. 5A, Fig. 1B). The substitution of Q in the QG(Q/I) sub-motif would also remove one of the unfavourable hydrophobic-hydrophilic interactions in the potential cross-seeded interface.

We expressed HEC in a *Δhet-s Δhellf* strain and tested the ability of the protein to propagate as a prion and to carry [Het-s] and/or [Φ] prion specificity *in vivo*. Strains expressing GFP-HEC showed two distinct phenotypes; [HEC*] strains presented diffuse GFP-HEC fluorescence, did not induce [Het-s] or [Φ] prions, and were unable to trigger cell death by incompatibility with HET-S or HELLF expressing strains (*SI Appendix*, Fig. S9, Table S6, Table S7). We observed that

some [HEC*] strains did, spontaneously and at low rate (~10%), transition into a [HEC] state characterized with the appearance of fluorescent dot-like aggregates (*SI Appendix*, Fig. S9, Table S6). None of the spontaneous [HEC] strains were able to induce [Het-s] or produce a barrage with a HET-S strain. Yet, [HEC] strains induced cell death with HELLF-expressing strains, indicating that the engineered HEC sequence shows [Φ] prion specificity and we termed the phenotype [HEC$^{\Phi}$] (Fig. 4B; *SI Appendix*, Fig. S9). We were equally able to induce the [HEC$^{\Phi}$] phenotype by exposing [HEC*] strains to [Φ] strains (*SI Appendix*, Table S7). Spontaneously formed (or [Φ]-induced) [HEC$^{\Phi}$] strains converted [HEC*] strains into [HEC$^{\Phi}$] prion state after contact, demonstrating the ability of aggregated HEC to self-propagate (behave as prion) (*SI Appendix*, Fig. S9).

Next, we found that after a contact with a [Het-s] strain, the prion-free [HEC*] strains could equally be converted to a [HEC] state, characterized by the appearance of fluorescent GFP-HEC dot-like aggregates and the ability to induce cell death with HELLF, indicating that the prion state of HEC can be induced both by HELLF and HET-s (*SI Appendix*, Table S7). Importantly, we found that [Het-s]-induced [HEC] strains, unlike the [HEC$^{\Phi}$] strains, were capable of converting [Het-s*] strains into [Het-s] strains and to induce cell death with HET-S (Fig. 5, B and C; *SI Appendix*, Fig. S9). Hence, we termed this phenotype [HEC^{S}]. Importantly, [HEC$^{\Phi}$] and [HEC^{S}] phenotypes remained stable in time and faithfully self-propagated over several passages (*SI Appendix*, Table S7, Table S8). In addition, we observed that GFP-HEC aggregates from [HEC^{S}] strains partially co-localized with [Het-s] and not with [Φ], while fluorescent HEC aggregates from [HEC$^{\Phi}$] strain produced the opposite results and co-localized predominantly with [Φ] (*SI Appendix*, Fig. S9). We concluded that the engineered HEC sequence could propagate as two distinct prion strains [HEC$^{\Phi}$] and [HEC^{S}] and was capable of breaching the cross-seeding barrier between [Het-s] and [Φ] prions. A likely explanation could be found in the reduced hydrophilic – hydrophobic clashes between HEC and the sequences of the two fungal prions (HET-s and HELLF), following the replacement of two strongly conserved hydrophilic HRAM5-specific residues (Q236 and Q263 in HELLF) with HRAM1-specific hydrophobic residues (L241 and

I277 in HET-s). Because HEC was designed by the targeted replacement of HRAM-specific residues, we concluded that such residues play a key role in the control of prion propagation, allowing or preventing cross-seeding between HRAM families.

Cross-seeding induced structural plasticity of HEC near HRAM-specific residues

To pinpoint determinants of the cross-seeding at structural level, we investigated the engineered protein sequence *in vitro* using ssNMR. Based on the resonance assignment of recombinant ^{13}C,^{15}N-labelled sample, HEC adopts a cross-β fold, highly similar to HET-s and HELLF (*SI Appendix*, Fig. S10, Fig. S11B). We then assembled HEC fibrils *in vitro* in presence of 5% of unlabelled HET-s or HELLF, respectively termed HEC^S and HEC^Φ. The resulting fibrillar states were analysed using solid-state NMR and the detected spectral fingerprints were similar between the three HEC preparations (HEC, HEC^S and HEC^Φ), while exhibiting slight structural differences at some amino acid positions (*SI Appendix*, Fig. S11). Both co-aggregation experiments (HEC + 5% HET-s and HEC + 5% HELLF) produced relatively similar chemical shift perturbations in HEC, suggesting similar interaction surfaces between the peptides (*SI Appendix*, Fig. S11). To gain further insight into the structural differences between HEC co-aggregated with HET-s or HELLF, we compared both chemical shift sets and plotted the differences as a function of the primary sequence (Fig. 5D). We detected small CA chemical shift variations on residues constituting the amyloid core of HEC^S and HEC^Φ, suggesting slight conformational changes within the assemblies (Fig. 5, D and E). Remarkably, most of the residues showing highest backbone chemical shift difference between HEC^S and HEC^Φ were part of or adjacent to the HRAM-defining positions that were modified in HELLF to engineer HEC (highlighted in red in Fig. 5D). Chemical shift differences are not only observed at the level of backbone conformation but also on side-chain NMR signals (e.g. M235 and F262). Additional NMR signals were observed (peak doubling, i.e. A223) between HEC^S / HEC^Φ and HEC (Fig. 5E) indicating a second local structural conformation for some residues (Fig. 5F). Considering chemical shift differences and presence of peak doubling, we observed that the QxFG and QG(Q/I) sub-motifs, which distinguish HELLF (HARM5) from HET-s (HRAM1) and have been

partially replaced in HELLF to engineer HEC, are the most impacted regions during the cross-seeding experiments of HEC (Fig. 5, Fig. 1B). Thus, the results indicate that the engineered HEC sequence adopts similar amyloid fold to HET-s and HELLF, while exhibiting limited structural plasticity near several different HRAM-specific residues during cross-seeding. Although these conformational changes are subtle, they are in agreement with the observed HEC prion strains *in vivo* and highlight the role of HRAM-specific residues as potential hotspots defining prion infectivity and controlling cross-seeding.

Discussion

Our study exploits the natural diversity occurring in a superfamily of fungal prion domains to document the limits of sequence-to-fold conservation in amyloids and the molecular and structural determinants of cross-seeding. First, by structurally characterizing highly divergent natural prion amyloids of the HRAM family, we uncovered that functional amyloids can evolve in a regime of fold conservation, withstanding extreme sequence diversification. Our work thus indicates that the sequence-to-fold evolutionary interplay for functional amyloids is similar to what has been described for globular (35) and membrane proteins (36) with fold conservation occurring even at very low levels of sequence identity and similarity. These findings are in agreement with previous studies documenting the high resistance of the β-solenoid fold to an extensive array of amino acids substitutions (32, 33). The apparent rigidity of β-solenoids has been proposed as a key feature for this class of proteins to perform as scaffolding devices (34). Here, the robustness of the β-solenoid fold would equally allow for the diversification of the HRAM signalling specificities (25).

The experimental HELLF SSNMR structure as well as the study of synthetic HRAM-derived proteins (HEC and HED) confirms structural and functional importance of the pattern of hydrophobic/polar side chain arrangement in HRAM families. This combination of bioinformatics and experimental approaches now opens the possibility to predictably engineer the generic HRAM β-solenoid fold.

Second, this study sheds light in an unprecedented way on the determinants of amyloid cross-seeding. We found that virtually identical amyloid backbone structures might not be sufficient for cross-seeding and that critical side-chain positions could determine the seeding specificity of an amyloid fold. Extrapolating our conclusions to amyloids causing neurodegeneration, especially considering the structural similarities between the HRAM β-solenoid fold and β-solenoid folds of pathological amyloids in humans (17, 18, 37, 38), provides a conceptual update on key features of the molecular behaviour for this category of pathogenic agents.

Materials and Methods

Prion propagation and incompatibility assays. Incompatibility phenotypes were determined by confronting strains of solid corn meal agar medium and a 'barrage' reaction was assessed 2-3 days post-contact. Prion propagation was assayed as the ability to transmit the [φ] prion phenotype from a [φ]-donor strain to a [φ*] prion-free tester strain after confrontation on solid medium. Transformants were confronted to wild type strains either directly or after contact with a [φ]-donor strain 6, 11 and 17 days after transfection to evaluate [φ*] and [φ] phenotypes frequencies and spontaneous [φ] prion propagation. Protein transfection experiments with amyloid fibrils of recombinant HELLF(209-277) or HET-s(218-289) were carried following the general protocol described by Benkemoun *et al.* (39) with minor modifications. In brief, an agar piece (~ 5 mm3) covered with fresh (24 h of growth) prion-free mycelium is placed in a 2 ml screw cap tube containing 500 µl of STC buffer (0.8 M sorbitol, 50 mM CaCl2, 100 mM Tris-HCl pH 7,5) in addition to 50 µl of amyloids (2-3 mg.ml-1). The mycelium is fragmented using a mechanical cell disruptor (FastPrepTM FP120). Two consecutive runs of 30 s each at speed of 6 m/s were realized and fractions of the suspension (20-25 µl) were directly spotted on corn meal medium to be assessed for prion conversion after 4-5 days of regeneration at 26°C.

Protein purification. Cells were sonicated on ice in a lysis buffer (Tris 50 mM, 150 mM NaCl, pH 8) and centrifuged to remove *E. coli* contaminants. Proteins were expressed in inclusion bodies due to their insoluble properties and purified under denaturing conditions. The supernatant

was discarded and the pellet incubated with lysis buffer supplemented with 2 % Triton X-100. The membrane pellet containing inclusion bodies was extensively washed with lysis buffer to remove Triton X-100 traces and incubated at 60 °C overnight with 8 M guanidine hydrochloride until complete solubilization. After a centrifugation step at 250 000 g, lysate was recovered and incubated for 2 h with pre-equilibrated Ni-NTA beads (Ni Sepharose 6 Fast Flow, GE Healthcare Life Sciences) in a binding buffer (50 mM Tris, 0.5 M NaCl, 20 mM imidazole, 7 M urea, pH 8). Proteins were eluted from the beads with 10 mL of elution buffer (50 mM Tris, 0.5 M NaCl, 500 mM imidazole, 7 M urea, pH 8). After the affinity chromatography step, proteins were loaded on a HiPrep 26/10 desalting column (GE Healthcare) to exchange buffer for 1 % acetic acid and remove low molecular weight compounds. All the purification steps were realized in 100 % H_2O. It allowed amide proton back exchange under denaturing conditions for the mixed (1/1) [(U-^{1}H/^{14}N)/(U-$^{1}H_N$/^{2}H/^{15}N)] sample.

***Assembly of HELLF(209-273) fibrils in vitro*.** The pure protein recovered after HPLC purification in 1% acetic acid was concentrated in Amicon Ultra-15 (cut-off 3 kDa) centrifugal filter units (Merck Millipore) to reach the final protein concentration of 1 mM. For the mixed (1/1) [(U-^{1}H/^{14}N)/(U-$^{1}H_N$/^{2}H/^{15}N)] sample, monomers were solubilized in 1% acetic acid at 1 mM concentration at a molar ratio of 1:1. Fibrils were formed by adjusting the pH with 3 M Tris to a pH value of 7.5. The protein solution was allowed to self-assemble for 2 weeks at room temperature under slow shaking. Fibrils were then centrifuged at 20000 g and washed several times with water supplemented with 0.02 % NaN_3 and transferred to the ssNMR rotor.

Solid-state NMR spectroscopy of HELLF(209-277). ssNMR spectra were recorded on a 23.5 T (1 GHz ^{1}H frequency) spectrometer (Bruker Biospin, Germany) equipped with a 0.7 mm triple resonance (^{1}H, ^{13}C, ^{15}N) MAS probe. Sample spinning frequency was 100 kHz. Spectra were referenced according to 4,4-dimethyl-4-silapentane-1-sulphonic acid (DSS) signals.

Backbone and side-chain resonances assignment of HELLF. We used a set of eight 3D ^{1}H detected experiments: (HCA)CB(CA)NH [4 scans, 11 ms (t3) x 4 ms (t2) x 20 ms (t1)], (HCO)CA(CO)NH [16 scans, 11 ms (t3) x 8 ms (t2) x 20 ms (t1)], (H)CANH [4 scans, 11 ms (t3) x

8 ms (t2) x 20 ms (t1)], (H)CONH [8 scans, 11 ms (t3) x 8 ms (t2) x 20 ms (t1)], (H)CO(CA)NH [32 scans, 11 ms (t3) x 8 ms (t2) x 20 ms (t1)], (HCA)CBCAHA [4 scans, 8 ms (t3) x 4 ms (t2) x 20 ms (t1)], (H)N(CO)CAHA [8 scans, 14 ms (t3) x 6 ms (t2) x 20 ms (t1)] and (H)NCAHA [4 scans, 14 ms (t3) x 8 ms (t2) x 20 ms (t1)]. The combination of these experiments allowed the connectivities between each ^{1}H-^{15}N couple to intra-residual or sequential CA, CA, CO and HA resonances, necessary to perform the entire backbone assignment. Side-chain proton assignment was performed using a ^{1}H-^{13}C CP-based sequence followed by a WALTZ mixing step (H)CwaltzCH [2 scans, 6 ms (t3) x 6 ms (t2) x 20 ms (t1)]. We used as a starting point the previously assigned CA and HA chemical shifts to correlate unambiguously all the carbons and protons of the side-chains step by step (27). Spectra were analysed using the CCPNmr Analysis Software (40).

Collection of intra- and inter-molecular restraints for HELLF from solid-state NMR. 211 distance restraints per monomer were collected from ^{1}H detected ssNMR spectra to determine the 3D structure of the HELLF(209-273) amyloid fibril. We added to these restraints 34 dihedral angles (phi/psi) estimated from chemical shifts using the TALOS+ software. 143 long-range intra-molecular restraints were assigned on 3D (H)CHH [4 scans, 6 ms (t3) x 4 ms (t2) x 20 ms (t1)], HhNH [8 scans, 8 ms (t3) x 4 ms (t2) x 20 ms (t1)] and H(H)CH [4 scans, 6 ms (t3) x 4 ms (t2) x 20 ms (t1)] spectra using a radio frequency-driven recoupling (RFDR) ^{1}H-^{1}H mixing. 33 inter-molecular restraints were assigned on a 3D H(H)NH spectrum [48 scans, 9 ms (t3) x 4 ms (t2) x 20 ms (t1)] using a RFDR ^{1}H-^{1}H mixing, using a mixed (1/1) [(U-^{1}H/^{14}N)/(U-$^{1}H_N$/^{2}H/^{15}N)] sample for the unambiguous detection of intermolecular restraints. A RFDR mixing followed by a ^{15}N-edited CP allowed a magnetization transfer from all the protons of the (U-^{1}H/^{14}N) HELLF monomers to ^{15}N atoms of the (U-$^{1}H_N$/^{2}H/^{15}N), back protonated monomers adjacent in the fibril, followed by the ^{1}H detection of the amide protons

NMR structure calculation of HELLF. The structure of HELLF fibrils was determined in several cycles of structure calculations and restraint analysis with ARIA 2.3 (41). Cross-peak assignments for ^{1}H-^{1}H correlations were converted into distance restraints with an upper-

bound of 8.5Å. Backbone dihedrals angles were predicted with TALOS+(30) from ^{1}H, ^{13}C and ^{15}N chemical shifts. TALOS predictions for residues in secondary structure elements (R1β_{1-4}, R2β_{1-4} and C-terminal α-helix) were converted in dihedral angle restraints with an error range corresponding to ± 1.5 times the TALOS error with a minimum of ± 15°. HELLF fibrils structure was calculated as a pentamer with five copies of HELLF(220-272) using simulated annealing performed with CNS 1.2 (42). The ladder topology was maintained during the calculation through distance restraints ensuring that the distance between equivalent Cα atoms in neighbouring monomers is constant throughout the pentamer, without fixing a particular distance value, i.e. $d_{m/m+1} = d_{m+1/m+2} = d_{m+2/m+3} = d_{m+3/m+4} = d_{m+4/m+5}$ (43, 44). Additionally, an NCS restraint was added to minimize the r.m.s difference between atomic coordinates of the monomers(44). For every ARIA iteration 100 structures were calculated and the 10 lowest-energy structures from the last iteration were refined in a shell of water molecules (45). On the basis of the identified β-strands and the in/out distribution of side-chains from an initial ARIA calculation using NMR restraints only, intra- and inter-monomer hydrogen bond restraints between equivalent β-strands from the R1 and R2 pseudo-repeats were included in subsequent rounds of ARIA calculation. Final restraints and structure statistics are given in SI Appendix, Table 3.

Solid-state NMR spectroscopy of HEC, HEC, HEC^{S} and HEC^{Φ} D. Proton-detected ssNMR spectra were recorded on a 23.5 T (1 GHz ^{1}H frequency) and 14.1 spectrometers (Bruker Biospin, Germany) equipped with 0.7 mm, 1.3 mm and 3.2 mm triple resonance (^{1}H, ^{13}C, ^{15}N) MAS probes. Spinning frequency was maintained at 100 kHz (0.7 mm) and 60 kHz (1.3 mm) for ^{1}H detection and 11 kHz (3.2 mm) for ^{13}C detection, respectively.

2D (H)NH experiments of HEC and HED were recorded at 100 kHz MAS (1 GHz ^{1}H frequency spectrometer). Resonance assignment of HED, recorded using a 1.3 mm probe (1 GHz ^{1}H frequency spectrometer), was performed using the following set of experiments: (H)CONH, (H)(CO)CA(CO)NH, (H)NCAH, (H)COCAH. 2D ^{13}C-^{13}C experiments of HEC^{S} and HEC^{Φ} were recorded at 11 kHz MAS (600 MHz ^{1}H frequency spectrometer).

Experimental data were processed using TopSpin and analyzed using Sparky (46) or CCPNMR.

Modeling of HRAMs families structures. 3D models of the prion forming domain (PFD) of representative proteins of HRAM-2, HRAM-3 and HRAM-4 were constructed with the program MODELLER (47) using the HET-s(218–289) (PDB 2KJ3) (43) and HELLF(220-272) structures. For each HRAM family, the sequence of the R1 and R2 repeats of HET-s and HELLF were aligned on the predicted repeats of the PFD to be modeled. HRAMs models were built as trimers using the atomic coordinates of the R1 and R2 repeats of HELLF and HET-s structures as templates.

Data Availability

All data from this work are included in the main text and the SI Appendix of the paper.

Acknowledgments

We acknowledge financial support from the European Research Council (ERC) under the European Unions Horizon 2020 research and innovation programme (ERC-2015-CoG GA no. 648974 to G.P. and ERC-2015-StG GA no. 639020 to A.L.), IdEx Bordeaux (Chaire d'Installation to B.H., ANR-10-IDEX-03-02), the ANR (ANR-14-CE09-0020-01 to A.L., ANR-13-PDOC-0017-01 to B.H. and ANR-17-CE11-0035 to S.J.S), the INCEPTION project (PIA/ANR-16-CONV-0005) and the CNRS (IR-RMN FR3050). J.S. and L.B.A. were supported by individual MSCA incoming fellowships (REA grant agreements n°661799 "COMPLEX-FAST-MAS" and n°624918 "MEM-MAS"). A.D. was supported by the Nouvelle Aquitaine Regional Council. We thank the Nouvelle Aquitaine Regional Council, the University of Bordeaux, and the CPER CampusB Bordeaux for the acquisition of the NMR equipment.

Author contributions

D.M., L.B.A., J.S., G.P., B.H., N. E.M and A.L. performed ssNMR experiments; D.M., N. E.M. G.P., B.H. and A.L. analyzed ssNMR data; B.B. implemented and performed structure calculations; D.M., M.B., A.N. expressed, purified, and polymerized HELLF fibrils for NMR; A.D., V.C., S.J.S. carried

out microscopy, prion infectivity and in vivo experiments; B.K. performed x-ray diffraction experiment; J.S.W. performed STEM experiments; A.D., D.M., B.H., A.L. and S.J.S. wrote the paper; all authors discussed the results and commented on the manuscript.

Declaration of Interests

The authors declare no competing financial interests.

Bibliography

1. Chiti F, Dobson CM (2017) Protein misfolding, amyloid formation, and human disease: A summary of progress over the last decade. *Annu Rev Biochem* 86:27–68.
2. Prusiner SB (2013) Biology and genetics of prions causing neurodegeneration. *Annu Rev Genet* 47:601–623.
3. Eisenberg D, Jucker M (2012) The amyloid state of proteins in human diseases. *Cell* 148(6):1188–1203.
4. Watts JC, Prusiner SB (2018) β-Amyloid Prions and the Pathobiology of Alzheimer's Disease. *Cold Spring Harb Perspect Med* 8(5).
5. Prusiner SB (2012) Cell biology. A unifying role for prions in neurodegenerative diseases. *Science* 336(6088):1511–1513.
6. Sanders DW, et al. (2014) Distinct tau prion strains propagate in cells and mice and define different tauopathies. *Neuron* 82(6):1271–1288.
7. Rey NL, et al. (2019) α-Synuclein conformational strains spread, seed and target neuronal cells differentially after injection into the olfactory bulb. *Acta Neuropathol Commun* 7(1):221.
8. Collinge J, Clarke AR (2007) A general model of prion strains and their pathogenicity. *Science* 318(5852):930–936.
9. Qiang W, Yau W-M, Lu J-X, Collinge J, Tycko R (2017) Structural variation in amyloid-β fibrils from Alzheimer's disease clinical subtypes. *Nature* 541(7636):217–221.
10. Morales R, Moreno-Gonzalez I, Soto C (2013) Cross-seeding of misfolded proteins: implications for etiology and pathogenesis of protein misfolding diseases. *PLoS Pathog* 9(9):e1003537.
11. Ren B, et al. (2019) Fundamentals of cross-seeding of amyloid proteins: an introduction. *J Mater Chem B, Mater Biol Med* 7(46):7267–7282.
12. Sampson TR, et al. (2020) A gut bacterial amyloid promotes α-synuclein aggregation and motor impairment in mice. *Elife* 9.
13. Horvath I, Wittung-Stafshede P (2016) Cross-talk between amyloidogenic proteins in type-2 diabetes and Parkinson's disease. *Proc Natl Acad Sci USA* 113(44):12473–12477.
14. Lim KH (2019) Diverse Misfolded Conformational Strains and Cross-seeding of Misfolded Proteins Implicated in Neurodegenerative Diseases. *Front Mol Neurosci* 12:158.
15. Ritter C, et al. (2005) Correlation of structural elements and infectivity of the HET-

s prion. *Nature* 435(7043):844–848.
16. Wasmer C, et al. (2008) Amyloid fibrils of the HET-s(218-289) prion form a beta solenoid with a triangular hydrophobic core. *Science* 319(5869):1523–1526.
17. Vázquez-Fernández E, et al. (2016) The structural architecture of an infectious mammalian prion using electron cryomicroscopy. *PLoS Pathog* 12(9):e1005835.
18. Fitzpatrick AWP, et al. (2017) Cryo-EM structures of tau filaments from Alzheimer's disease. *Nature* 547(7662):185–190.
19. Daskalov A, et al. (2015) Signal transduction by a fungal NOD-like receptor based on propagation of a prion amyloid fold. *PLoS Biol* 13(2):e1002059.
20. Riek R, Saupe SJ (2016) The HET-S/s Prion Motif in the Control of Programmed Cell Death. *Cold Spring Harb Perspect Biol* 8(9).
21. Saupe SJ (2011) The [Het-s] prion of Podospora anserina and its role in heterokaryon incompatibility. *Semin Cell Dev Biol* 22(5):460–468.
22. Seuring C, et al. (2012) The mechanism of toxicity in HET-S/HET-s prion incompatibility. *PLoS Biol* 10(12):e1001451.
23. Greenwald J, et al. (2010) The mechanism of prion inhibition by HET-S. *Mol Cell* 38(6):889–899.
24. Loquet A, Saupe SJ (2017) Diversity of amyloid motifs in NLR signaling in fungi. *Biomolecules* 7(2).
25. Daskalov A, Dyrka W, Saupe SJ (2015) Theme and variations: evolutionary diversification of the HET-s functional amyloid motif. *Sci Rep* 5:12494.
26. Agarwal V, et al. (2014) De novo 3D structure determination from sub-milligram protein samples by solid-state 100 kHz MAS NMR spectroscopy. *Angew Chem Int Ed Engl* 53(45):12253–12256.
27. Andreas LB, et al. (2016) Structure of fully protonated proteins by proton-detected magic-angle spinning NMR. *Proc Natl Acad Sci USA* 113(33):9187–9192.
28. Samoson A (2019) H-MAS. *J Magn Reson* 306:167–172.
29. Stanek J, et al. (2016) NMR Spectroscopic Assignment of Backbone and Side-Chain Protons in Fully Protonated Proteins: Microcrystals, Sedimented Assemblies, and Amyloid Fibrils. *Angew Chem Int Ed Engl* 55(50):15504–15509.
30. Shen Y, Delaglio F, Cornilescu G, Bax A (2009) TALOS+: a hybrid method for predicting protein backbone torsion angles from NMR chemical shifts. *J Biomol NMR* 44(4):213–223.
31. Loquet A, Giller K, Becker S, Lange A (2010) Supramolecular interactions probed by 13C-13C solid-state NMR spectroscopy. *J Am Chem Soc* 132(43):15164–15166.
32. Daskalov A, et al. (2014) Contribution of specific residues of the β-solenoid fold to HET-s prion function, amyloid structure and stability. *PLoS Pathog* 10(6):e1004158.
33. Wan W, Stubbs G (2014) Fungal prion HET-s as a model for structural complexity and self-propagation in prions. *Proc Natl Acad Sci USA* 111(14):5201–5206.
34. Kajava AV, Steven AC (2006) Beta-rolls, beta-helices, and other beta-solenoid proteins. *Adv Protein Chem* 73:55–96.
35. Rost B (1999) Twilight zone of protein sequence alignments. *Protein Engineering Design and Selection* 12(2):85–94.
36. Olivella M, Gonzalez A, Pardo L, Deupi X (2013) Relation between sequence and structure in membrane proteins. *Bioinformatics* 29(13):1589–1592.
37. Falcon B, et al. (2018) Structures of filaments from Pick's disease reveal a novel tau protein fold. *Nature* 561(7721):137–140.
38. Falcon B, et al. (2019) Novel tau filament fold in chronic traumatic

encephalopathy encloses hydrophobic molecules. *Nature* 568(7752):420–423.
39. Benkemoun L, et al. (2006) Methods for the in vivo and in vitro analysis of [Het-s] prion infectivity. *Methods* 39(1):61–67.
40. Stevens TJ, et al. (2011) A software framework for analysing solid-state MAS NMR data. *J Biomol NMR* 51(4):437–447.
41. Bardiaux B, Malliavin T, Nilges M (2012) ARIA for solution and solid-state NMR. *Methods Mol Biol* 831:453–483.
42. Brunger AT (2007) Version 1.2 of the Crystallography and NMR system. *Nat Protoc* 2(11):2728–2733.
43. Van Melckebeke H, et al. (2010) Atomic-resolution three-dimensional structure of HET-s(218-289) amyloid fibrils by solid-state NMR spectroscopy. *J Am Chem Soc* 132(39):13765–13775.
44. Nilges M (1993) A calculation strategy for the structure determination of symmetric dimers by 1H NMR. *Proteins* 17(3):297–309.
45. Linge JP, Williams MA, Spronk CAEM, Bonvin AMJJ, Nilges M (2003) Refinement of protein structures in explicit solvent. *Proteins* 50(3):496–506.
46. Lee W, Tonelli M, Markley JL (2015) NMRFAM-SPARKY: enhanced software for biomolecular NMR spectroscopy. *Bioinformatics* 31(8):1325–1327.
47. Sali A, Blundell TL (1993) Comparative protein modelling by satisfaction of spatial restraints. *J Mol Biol* 234(3):779–815.
48. Daskalov A, Paoletti M, Ness F, Saupe SJ (2012) Genomic clustering and homology between HET-S and the NWD2 STAND protein in various fungal genomes. *PLoS One* 7(4):e34854.

Fig. 1 HELLF is a distant HET-s homolog encoded in the genome of *Podospora anserina*.

A. Sequence similarity between HELLF and HET-s PFDs. The two pseudo-repeats are boxed. Conserved residues are shown in Taylor colour scheme and intensity of colour reflects degree of conservation. **B.** MEME cartoons showing the conservation of HRAM-specific residues. **C.** Dot-like aggregates of the HELLF PFD (GFP-HELLF(209-277)) formed in *P. anserina*. Scale bar is 5 μm. **D.** HELLF controls a programmed cell death reaction as determined by the 'barrage' phenotype (white arrowhead) between strains expressing full-length HELLF and strains expressing the HELLF PFD in the [φ] prion state. **E.** Electron micrograph of fibrillar assemblies of the HELLF PFD, scale: 100nm.

Fig. 2 Solid-state NMR (ssNMR) characterization of HELLF(209-277) fibrils. A. ssNMR sample preparation of HELLF(209-277), requiring minimal sample quantity (<300ug) using a 0.7 mm ssNMR rotor. **B.** Extracts of ssNMR spectra for ^{1}H, ^{13}C and ^{15}N sequential assignments. A combination of (HCA)CB(CA)NH (red), (HCO)CA(CO)NH (black), (H)CANH (purple), (H)CONH (green) and (H)CO(CA)NH (blue) was used to assign HELLF(209-277) fibrils. **C.** ^{1}H-^{13}C ssNMR spectra of fully protonated HELLF(209-277) amyloid fibrils. **D-F.** Collection of ssNMR distance restraints. **D.** Intramolecular distances based on a H…(H)CH experiment on fully protonated HELLF sample. **E.** ssNMR approach to detect intermolecular interactions, based on a (1/1) [(U-$^{1}H/^{14}N$)/(U-$^{1}H_N/^{2}H/^{15}N$)]-labelled HELLF sample. **F.** Intermolecular distances based on a H…(H)NH experiment on (1/1) [(U-$^{1}H/^{14}N$)/(U-$^{1}H_N/^{2}H/^{15}N$)]-labelled HELLF(209-277). **G.** ssNMR restraints shown on the HELLF(209-277) rigid core.

Fig. 3 Solid-state NMR structure of HELLF(209-277) amyloid assembly. A. Side view of a ribbon representation of HELLF(209-277) structure, representing five monomers stacked in the fibrillar arrangement. Individual molecules are represented in different colours. **B.** Top view of the SSNMR HELLF(209-277) amyloid structure with main fibril axis and labelled β-strands. **C.** Top view of the solenoid-forming pseudo-repeats, R1 (top) and R2 (bottom), of HELLF(209-277). Hydrophobic residues are shown in white, acidic residues in red, basic residues in blue and others green.

Fig. 4 HELLF(209-277) amyloid fold presents strong similarity with HET-s(218-289),

while the two prion domains lack *in vivo* cross-seeding. A. Backbone structural alignment of HELLF PFD (in blue) and HET-s PFD (in yellow) ssNMR structures. **B-C.** Shown are four cartoons representing the hydrophobic triangular core of amyloid fibrils formed by the successively stacked pseudo-repeats – R1 (left panels) and R2 (right panels) – of HELLF (**B**) and of HET-s (**C**). Amino acid residues decorating the amyloid backbones are drawn as beads of different colours. Hydrophobic residues are shown in white, acidic residues in red, basic residues in blue and others green. **D.** Fluorescent microscopy images of strains co-expressing HET-s-RFP ([Het-s*] or [Het-s] state) and the cytotoxic-dead HELLF(L52K)-GFP mutant ([Φ*] or [Φ] state) exhibiting distinct epigenetic combinations. Full panels are given in SI Appendix, Fig. S8. Scale bar: 2 μm. **E.** 3D models for the two pseudo-repeats of different HRAM families. Below the molecular models are shown the protein sequences used to generate the models for each HRAM family. The sequences GenBank/NCBI reference IDs are as follows: XP_009252118.1 (HRAM1), CDM29511.1 (HRAM2), XP_007744431.1 (HRAM3) and XP_007838484.1 (HRAM4).

Fig. 5 HELLF-derived chimeric protein HEC breaches the prion cross-seeding barrier between HELLF and HET-s. A. Sequence alignments of the two pseudo-repeats (R1 and R2), constituting the PFDs of HELLF, HET-s and the engineered protein HEC. HELLF-specific residues are shown in blue colour. HET-s-specific HRAM1-defining residues are shown in red. Residues shared between all three proteins are shown in purple. **B.** Representation of barrage phenotypes between strains expressing full-length HET-S or HELLF in confrontations with HEC-expressing strains of [HEC^{S}] (carrying HEC prion strain induced by contact with [Het-s] prion) or [HEC$^{\Phi}$] (HEC prion strain induced by [Φ]) phenotypes. The barrage reaction is shown as a line separating two incompatible strains (green circles). **C.** Induction of the [Het-s] prion by HEC-expressing strains *in vivo*. [Het-s] induction is measured in percentage of prion-free [Het-s*] strains converted (by the cited strains) to prion-infected [Het-s] strains. Negative control is

indicated with a minus sign. Experiments were performed at least in triplicate. P value ($a \neq b$) < 0.0001, one-way ANOVA with Tukey's multiple comparisons test. **D.** Cα chemical shift differences between HEC seeded with [Het-s] and [Φ]. Non-identical residues between HEC and HELLF are coloured in red. Asterisks indicate unassigned residues because of spectral ambiguities. **E.** Extracts of ^{13}C-^{13}C ssNMR spectra of HEC fibrils seeded with [Het-s] (red) or [Φ] (blue). **F.** Cartoon representation of the amyloid backbone of HEC pseudo-repeats. Residues with highest conformational changes between HEC seed by HET-s or HELLF, as measured by difference in chemical shift on Cα, are shown in yellow. Green stars highlight residues in two conformations.

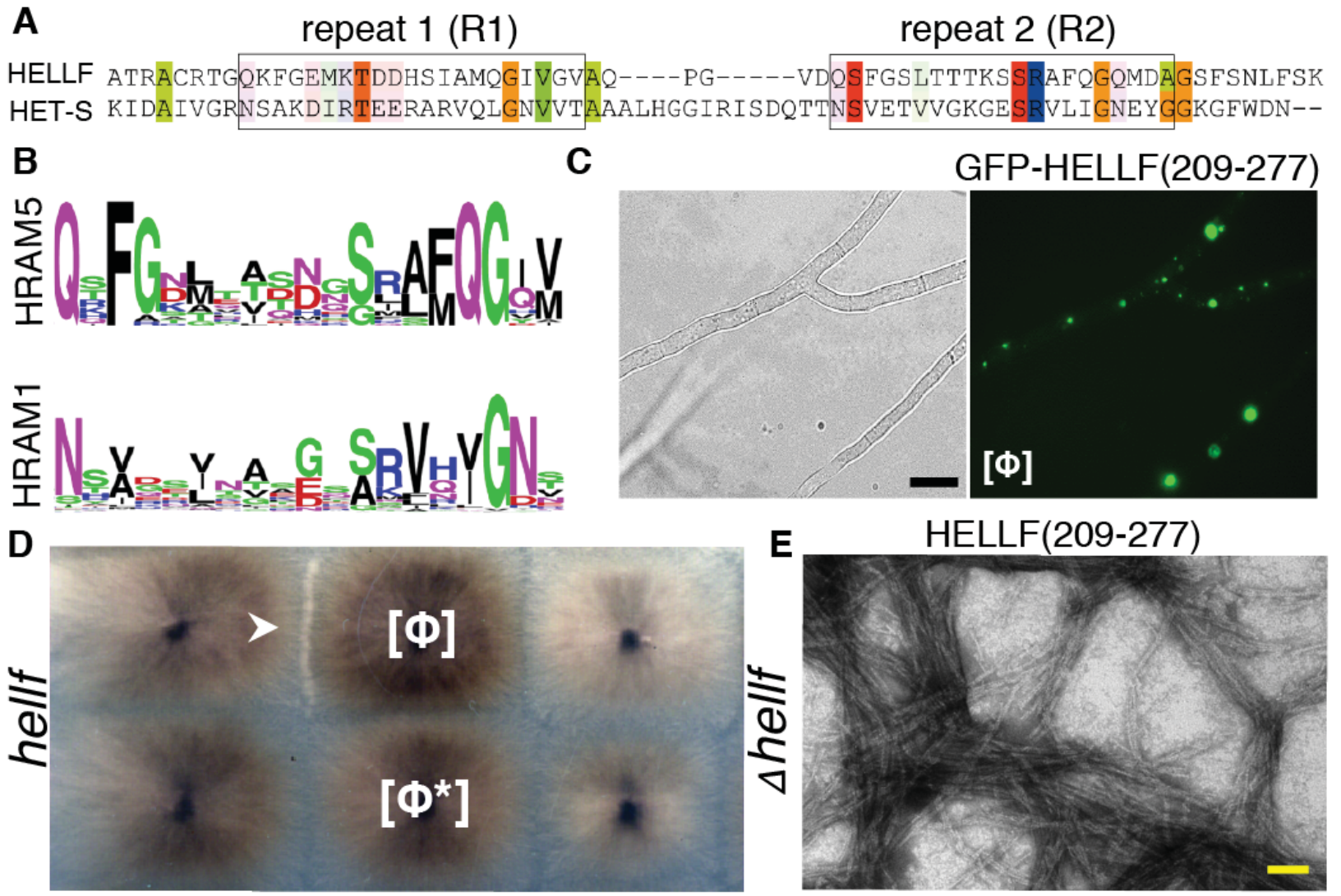
A
repeat 1 (R1)
repeat 2 (R2)
HELLF ATRACRTGQKFGEMKTDDHSIAMQGIVGVAQ----PG-----VDQSFGSLTTTKSSRAFQGQMDAGSFSNLFSK
HET-S KIDAIVGRNSAKDIRTEERARVQLGNVVTAAALHGGIRISDQTTNSVETVVGKGESRVLIGNEYGGKGFWDN--
B
HRAM5
HRAM1
C
GFP-HELLF(209-277)
[Φ]
D
hellf
[Φ]
[Φ*]
E
HELLF(209-277)
Δhellf

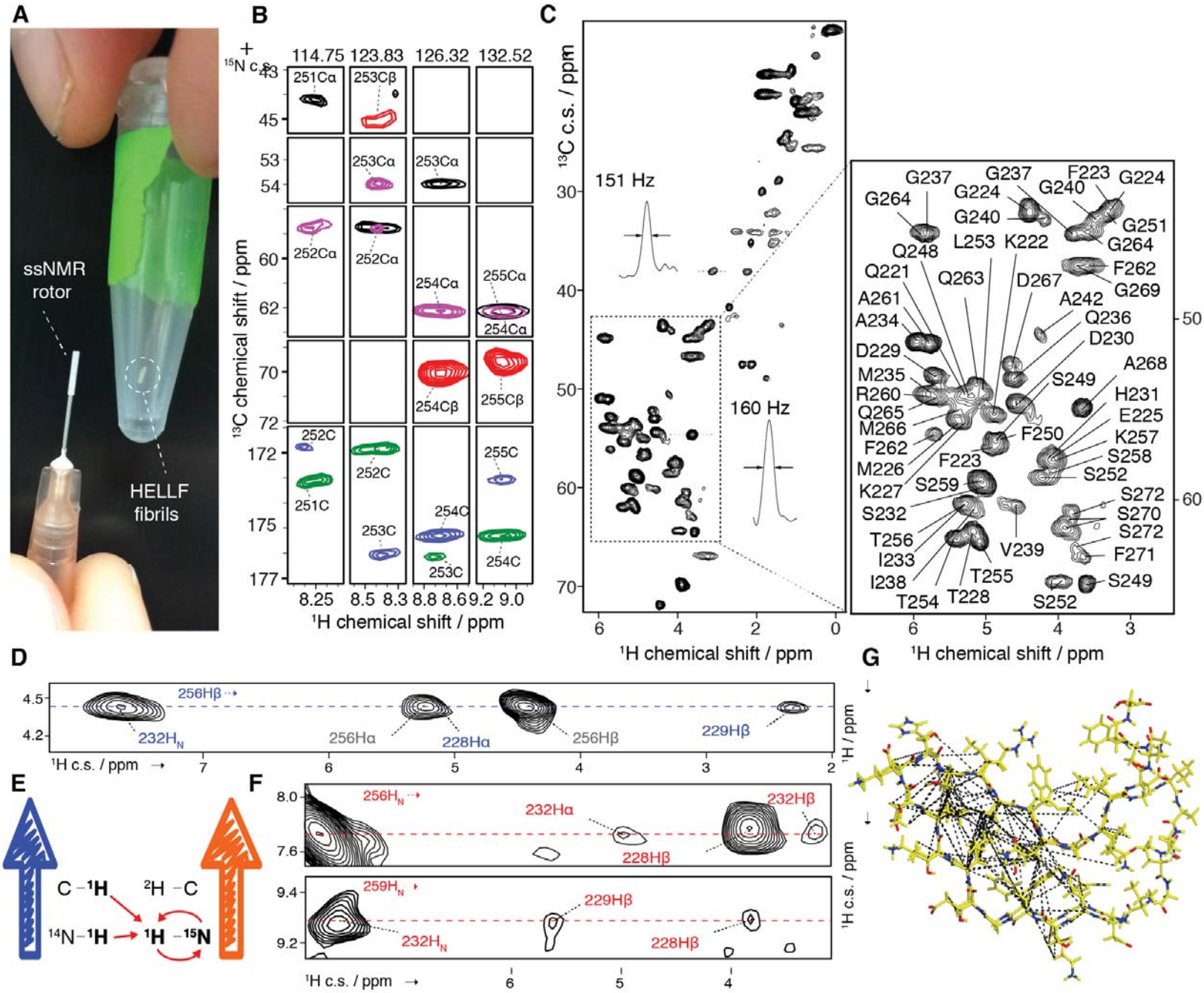
A
ssNMR rotor
HELLF fibrils
B
114.75 123.83 126.32 132.52
15N c.s.
251Cα
253Cβ
253Cα
252Cα
254Cα
255Cα
254Cβ
255Cβ
252C
251C
254C
255C
13C chemical shift / ppm
1H chemical shift / ppm
C
13C c.s. / ppm
151 Hz
160 Hz
1H chemical shift / ppm
G237 G237 F223 G224
G264 G224 G240
G240 G251
Q248 L253 K222 G264
Q221 Q263 D267 F262
A261 A242 G269
A234 Q236
D229 D230
M235 A268
R260 S249
Q265 H231
M266 E225
F262 F250 K257
M226 F223 S258
K227 S259 S252
S232 S272
T256 S270
I233 V239 S272
I238 F271
T254 T228 T255 S249
S252
1H chemical shift / ppm
D
256Hβ
232HN
256Hα
228Hα
256Hβ
229Hβ
1H c.s. / ppm
E
C –1H
2H –C
14N–1H
1H –15N
F
256HN
232Hα
232Hβ
228Hβ
259HN
229Hβ
232HN
228Hβ
1H c.s. / ppm
G
1H / ppm
1H c.s. / ppm

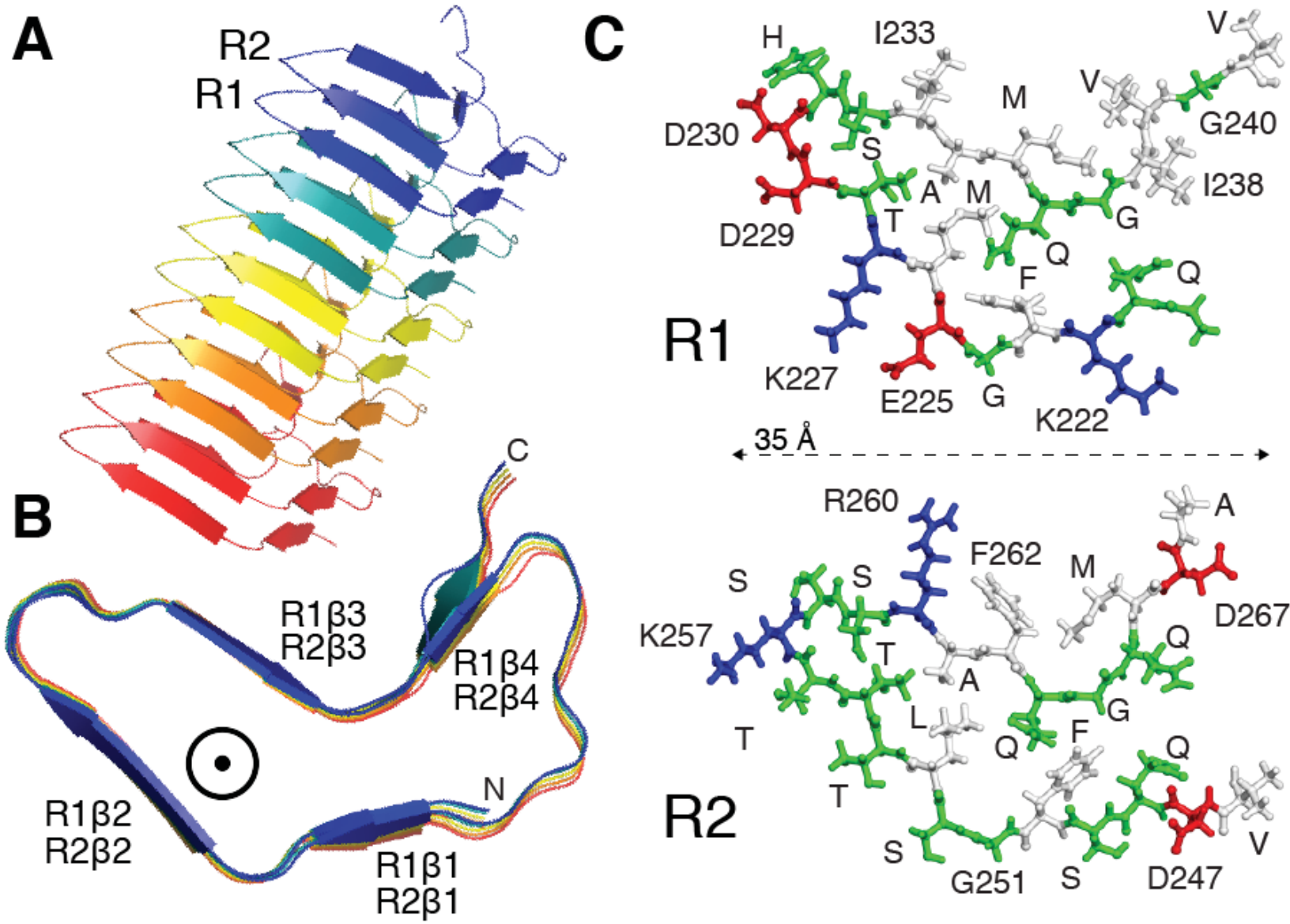
A
R2
R1
B
C
R1β3
R2β3
R1β4
R2β4
R1β2
R2β2
R1β1
R2β1
N
C
H
I233
V
V
M
G240
D230
S
I238
A
M
D229
T
G
Q
F
Q
R1
K227
E225
G
K222
35 Å
R260
A
F262
M
S
S
D267
K257
Q
T
A
G
L
T
Q
F
Q
T
R2
S
G251
S
D247
V

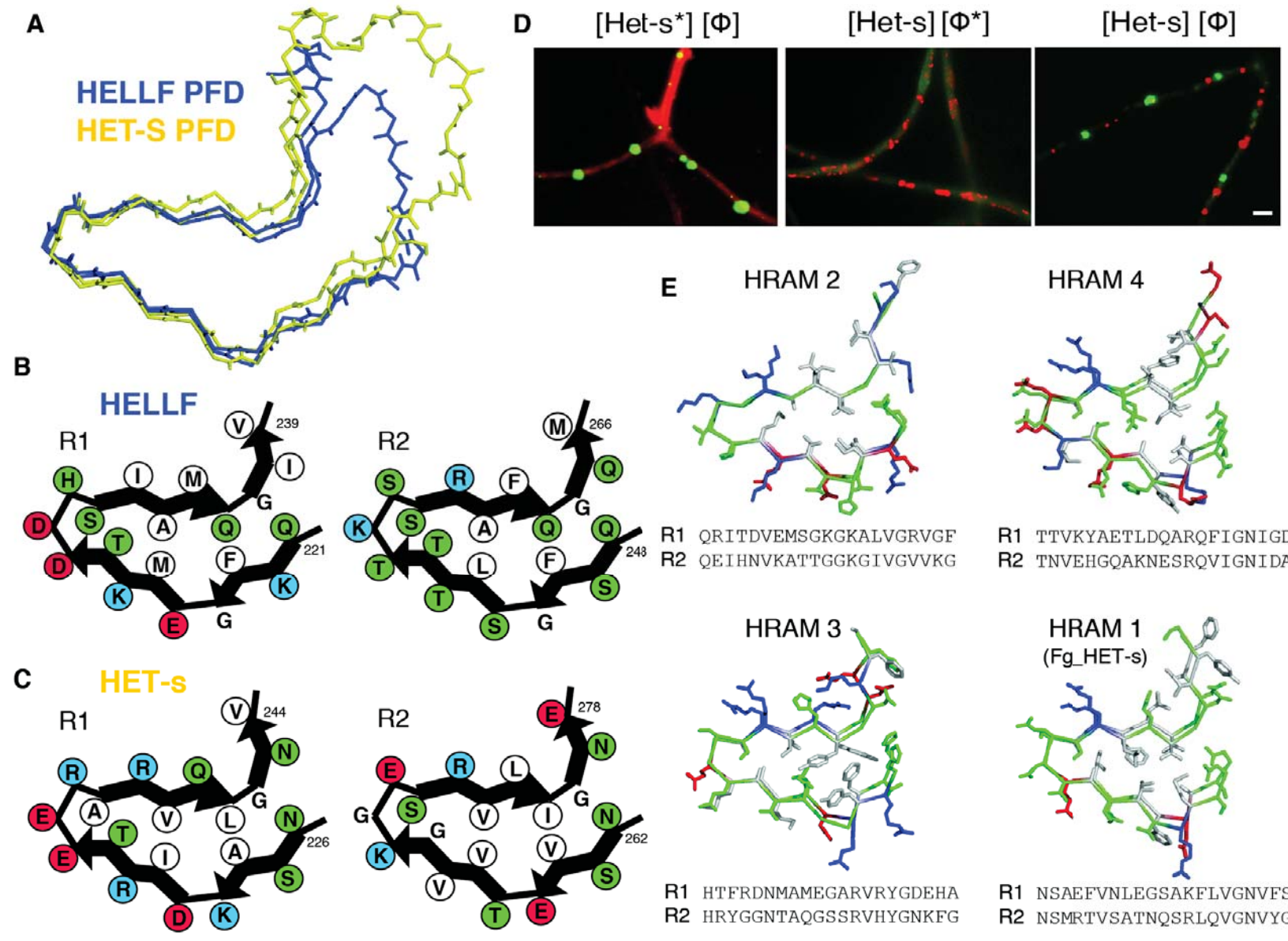
A
HELLF PFD
HET-S PFD
D
[Het-s*] [Φ]
[Het-s] [Φ*]
[Het-s] [Φ]
B
HELLF
R1
R2
C
HET-s
R1
R2
E
HRAM 2
HRAM 4
HRAM 3
HRAM 1
(Fg_HET-s)
R1 QRITDVEMSGKGKALVGRVGF
R2 QEIHNVKATTGGKGIVGVVKG
R1 TTVKYAETLDQARQFIGNIGD
R2 TNVEHGQAKNESRQVIGNIDA
R1 HTFRDNMAMEGARVRYGDEHA
R2 HRYGGNTAQGSSRVHYGNKFG
R1 NSAEFVNLEGSAKFLVGNVFS
R2 NSMRTVSATNQSRLQVGNVYG

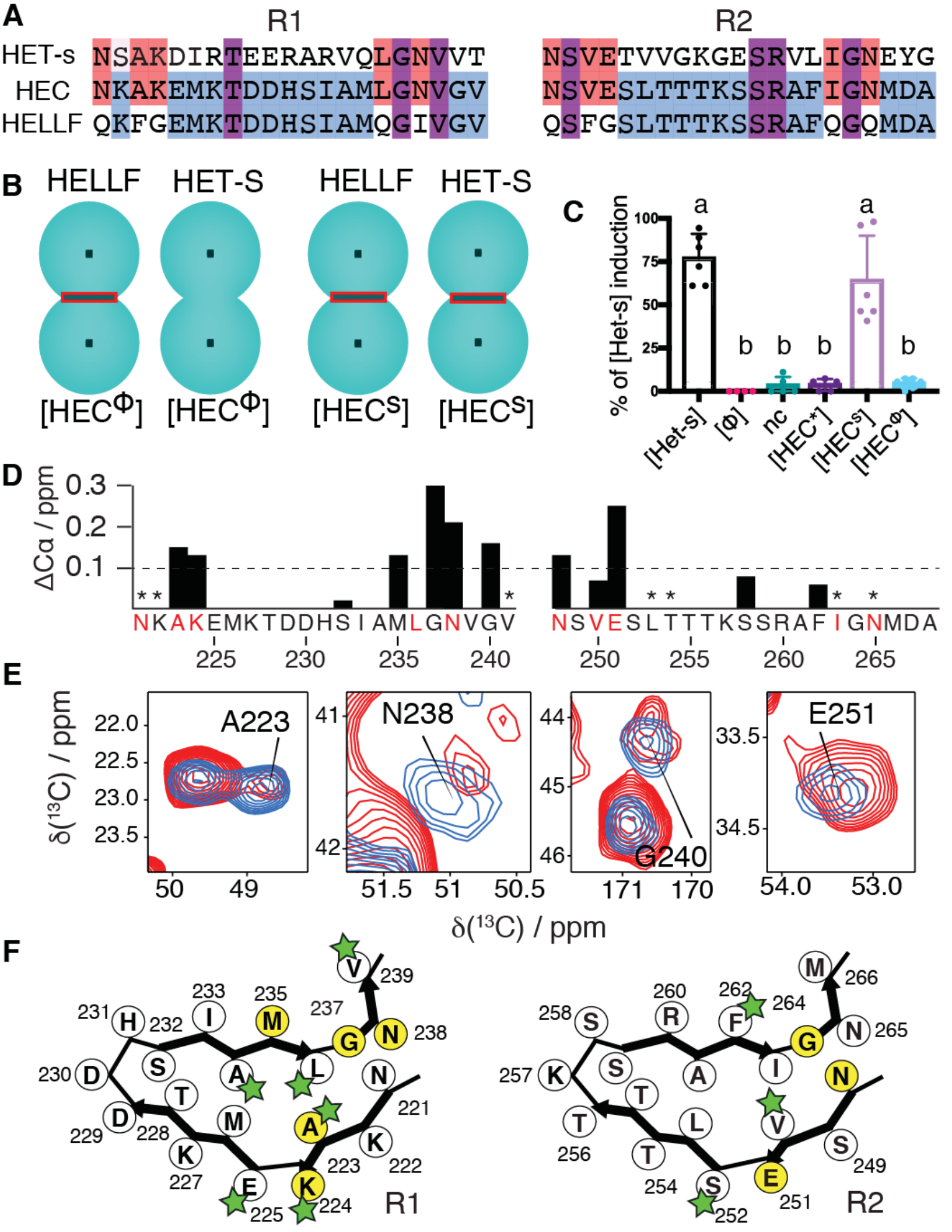
A
R1
R2
HET-s NSAKDIRTEERARVQLGNVVT NSVETVVGKGESRVLIGNEYG
HEC NKAKEMKTDDHSIAMLGNVGV NSVESLTTTKSSRAFIGNMDA
HELLF QKFGEMKTDDHSIAMQGIVGV QSFGSLTTTKSSRAFQGQMDA
B
HELLF
HET-S
HELLF
HET-S
[HECΦ]
[HECΦ]
[HECS]
[HECS]
C
% of [Het-s] induction
100
75
50
25
0
a
b
b
b
a
b
[Het-s]
[Φ]
nc
[HEC*]
[HECS]
[HECΦ]
D
ΔCα / ppm
0.3
0.2
0.1
NKAKEMKTDDHSIAMLGNVGV
NSVESLTTTKSSRAFIGNMDA
225
230
235
240
250
255
260
265
E
δ(13C) / ppm
A223
N238
G240
E251
22.0
22.5
23.0
23.5
41
42
44
45
46
33.5
34.5
50
49
51.5
51
50.5
171
170
54.0
53.0
δ(13C) / ppm
F
R1
R2